SUPPLEMENTARY INFORMATION

TABLE OF CONTENTS

1. Experimental Details

1.a. Experimental set up

The experimental set up is schematically depicted in Fig. S1. All components (except for the collinear pump-laser in-coupling) are part of the Liquid Jet Experiment (LJE) end station which is described in detail in ref. 31. For the measurements shown here, it was installed at the Soft X-Ray materials science (SXR) instrument[32, 33] of the Linac Coherent Light Source (LCLS)[34] at the SLAC National Accelerator Laboratory (SLAC) in Stanford, USA.
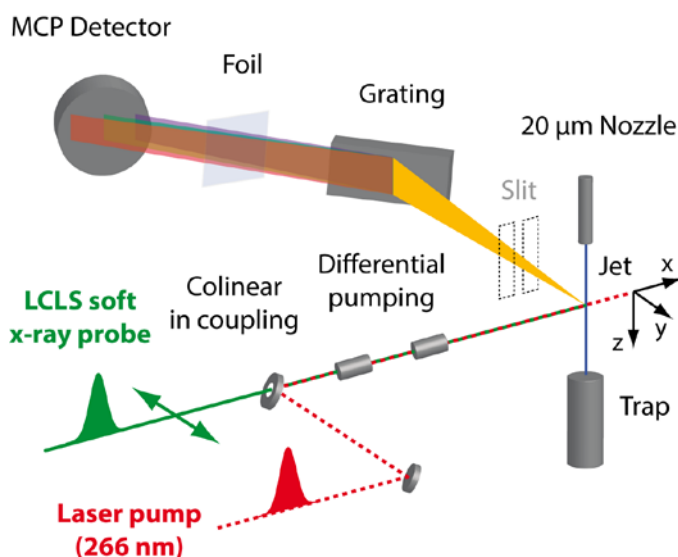
Supplementary Information Figure S1: Schematic depiction of the experimental set up. Details are given in the text and in ref. 31.

Fig. S1 details the preparation of the liquid sample in vacuum with a jet, the differential pumping to decouple the vacuum in the experimental vacuum chamber and the SXR beamline (not shown), the pump-probe scheme with optical excitation (pump at 266 nm) of the sample and soft x-ray probing (LCLS pulses with variable energy across the Fe L_3-absorption edge). Laser pump and x-ray probe pulses are in-coupled collinearly into the experimental vacuum chamber with a holey mirror on the x-ray propagation axis. The sample is prepared in vacuum with a liquid jet (diameter 20 μm) and frozen after the interaction region in a cold trap (see details below for sample preparation). Scattered photons resulting from resonant inelastic x-ray scattering (RIXS) at the Fe L_3-edge are detected and analyzed with a high-resolution RIXS spectrometer ("XES 350") consisting of a grating and a position-sensitive detector (multi-channel-plate, MCP, stack with fluorescence screen and glass viewport with a charge-coupled device, CCD, camera outside vacuum, details of data acquisition are reported below). RIXS is detected (along the y-axis in Fig. S1) at an angle of 90° with respect to the propagation direction of the x-ray beam (x axis in Fig. S1). X-ray propagation direction and RIXS-detection direction define the scattering plane (x-y plane).

The x-ray radiation is linearly polarized and the polarization axis (y axis) is parallel to the scattering plane. The entrance slit of the RIXS spectrometer (indicated in Fig. S1) is kept open to ensure maximum count rate. In this "slit-less mode" of operation, the intersection of the liquid jet and the incident x-ray beam defines the source volume of the spectrometer. A foil is used to decouple the vacuum in the MCP-detector housing and the jet chamber.

1.b. Sample preparation

The sample consisted of a 1mol/l solution of $Fe(CO)_5$ (ironpentacarbonyl, liquid at room temperature) in ethanol. The sample was run through an HPLC system including a degasser to form a liquid jet in vacuum[33] and collected after interaction with the x-ray beam in a cooling trap. $Fe(CO)_5$ of high purity (99 %) and ethanol (99%, Uvasol/spectrophotometric grade) were purchased from Sigma-Aldrich and used without further purification. Special care was taken in general to avoid exposure of the sample to light, air and elevated temperatures. In particular, the solution was prepared under a fume hood in a light protective flask, kept at all times below room temperature and continuously flushed with nitrogen gas. During the measurements, the solution was continuously flushed with nitrogen gas and kept below room temperature in light-secure bottles.

1.c. Experimental procedures

Spatial overlap of pump and probe pulses was established by overlaying the spots of both beams on a Ce:YAG screen installed in the experimental vacuum chamber in the plane of the liquid jet (y-z plane in Fig. S1).

Temporal overlap was first established on a coarse 5 ps time scale with a copper photocathode (in-vacuum SMA antenna) and subsequently on the femtosecond time scale with x-ray pump induced reflectivity changes on a SiN surface probed by the 266 nm optical-laser pulses[35, 36]. The SiN sample was mounted in the experimental vacuum chamber close to the liquid jet. The temporal resolution of this measurement and that of the reported time-resolved RIXS measurements was determined by the single x-ray pulse duration of 160 fs (FWHM, the LCLS electron bunch charge was 250 pC) and the arrival-time jitter between pump-laser and LCLS x-ray probe pulses. We found the overall temporal resolution of the experiment to be 300 fs as deduced from the fastest measured delay scans.

The sample was photo-excited by the third harmonic of the Ti:sapphire laser system at 266 nm (4.66 eV) of the SXR instrument (repetition rate 60 Hz). The pump-laser pulse

duration amounted to 100 fs (FWHM) and the pulse energy was estimated to ~5 μJ. With a pump-laser spot size of 100 x 400 μm^2 (horizontal x vertical, y and z-axes, respectively, in Fig. S1) this corresponded to a peak fluence of ~$1.25 \cdot 10^{11}$ W/cm^2. We found no evidence for multi-photon processes at this fluence of the pump laser.

Fe L$_3$-RIXS intensities were measured by scanning the incident photon energy from 703 to 715 eV and analyzing the energy of the scattered photons. The resolution in the RIXS measurements along the incident-photon energy axis is defined by the excitation bandwidth. This amounted here to 0.5 eV (FWHM) and was determined by the slit size of 150 μm of the SXR monochromator (first negative order of the monochromator grating with 100 lines/mm).

The average bandwidth of the LCLS radiation at the Fe L$_3$-edge was approximately 1% (7 eV)[34]. To cover the whole range of 12 eV for the incident photons, the LCLS electron beam energy was continuously scanned in an appropriate range. A script was used that adjusts the accelerator and the electron beam optics accordingly ("Vernier-scan"). The scan had a triangular shape with a four minute period. The beam line monochromator was set to follow this scan so that the selected photon energy was always centered on the amplification profile of the machine. This procedure ensures homogeneous average flux of monochromatized photons over the whole extended photon energy range.

The incident photon energy was calibrated using a calibrated Fe L-edge x-ray absorption spectrum of Fe(CO)$_5$ in ethanol (1 mol/l) measured at the synchrotron radiation facility BESSYII, Germany. There, the incident photon energy was calibrated with respect to the water O K-edge x-ray absorption spectrum with the pre-edge peak at 535 eV[37, 38]. The Fe L-emission-energy scale was calibrated using elastically scattered x-rays of known energy. The resolution of the RIXS spectra along the energy-transfer axis is defined by the resolution of the RIXS spectrometer. In the "slit-less mode" of operation of the spectrometer as used here (see above), this is defined by the diameter of the jet (20 μm)[39, 31] and it amounted to 1.0 eV[31].

RIXS intensities were normalized to the incident flux which was measured on a shot-to-shot basis with an intensity monitor installed after the SXR monochromator exit slit (the so-called "fluence monitor" described in ref. 33 consisting of a metal-coated semi-transparent membrane generating charge pulses as the x-ray pulses transmit). An additional calibration of relative intensities of this monitor was performed during the experiment by the integrated RIXS intensities at constant incident photon energy and time delay.

The employed average fluence of the incident monochromatized x-ray pulses on the sample was 30 mJ/cm^2 per pulse ($1.6 \cdot 10^{10}$ photons per pulse). In order to achieve this, the LCLS beam was attenuated by a factor of 10 with a gas attenuator installed upstream of the SXR beamline monochromator (the average unattenuated and unmonochromatized pulse energy amounted to 1.7 mJ). An x-ray spot size of 20 x 300 μm^2 (horizontal x vertical, y and z-axes, respectively, in Fig. S1) was used. This elongation along the liquid jet was chosen as to additionally reduce the photon density on the sample[31]. Finally, pulses with x-ray intensities above 100 mJ/cm^2 were discarded in the data analysis. In this way, spectral distortions observed in the Fe(CO)$_5$ RIXS spectra at high peak fluences could be avoided.

With the liquid-jet flow rate of 1 ml/min a sample volume of 20 x 300 μm^2 (horizontal x vertical, corresponding to the x-ray spot size) was replaced at a rate of 0.2 MHz guaranteeing that each x-ray probe pulse (repetition rate 60 Hz) hit a fresh volume of the sample.

The x-rays diffracted of the grating were converted to electrons and amplified by an MCP stack and subsequently converted to visible photons on a fluorescence screen. Outside vacuum, these photons were detected with a CCD camera (OPAL 1000 Adimec) that was synchronized with LCLS. For the time-resolved RIXS measurements, the monochromator (incident energy) and the delay stage (pump-probe delay) were continuously scanned. Their settings were recorded with the CCD image for each x-ray pulse separately and the data were sorted a posteriori according to incident energy and delay time. For further analysis, the raw data were binned in energy transfer, incident-photon energy and time delay. The bin sizes for negative (positive) delays are 0.2 (0.6) eV for the energy transfers and 0.2 (0.4) eV for the incident-photon energy. The bin size for the time delay is 0.2 ps. The average RIXS count rate for Fe(CO)$_5$ at negative delays per energy-transfer, incident-photon energy and time-delay bin (Fig. 1c of the main text) amounted to 0.9 counts/pulse for an incident photon energy at the maximum of the Fe L$_3$-absorption resonance at 711.5 eV. This is well within the linear regime of the detection system but we note that its multi-hit capability is essential. The average count rates for the transient signals (averaged over all positive delays) in regions 1, 2 and 3 (Fig. 2a in the main text) amounted to 0.001, 0.007 and 0.003 counts/pulse, respectively. The total accumulation time of the data reported here was 19 hours.

1.d. Deduction of the scaling factor for the measured difference RIXS maps in Fig. 1c (main text)

As the measured changes in the Fe L_3-RIXS data due to pump-laser induced dynamics (appearance of transients) are comparably small and the measured RIXS intensities are dominated by un-pumped ground-state $Fe(CO)_5$ signals, we show RIXS intensity differences in Fig. 1c of the main text to illustrate the time-dependent changes. Note that any quantitative information and in particular the deduction of the populations of intermediate species with the kinetic model were extracted from the raw data.
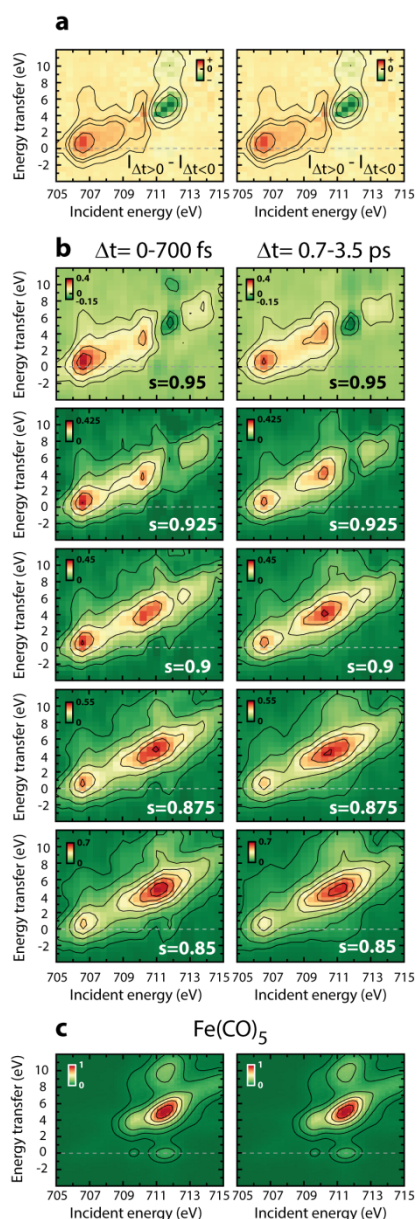
Supplementary Information Figure S2: Measured Fe L_3-edge RIXS intensities and RIXS intensity differences for varying scaling factors used to scale the ground-state $Fe(CO)_5$ intensities in the subtractions. The RIXS intensity is encoded in color (see color bar) and plotted versus energy transfer and incident photon energy. **a** Difference RIXS intensities (integrated intensities of all positive pump-probe delays minus integrated intensities of all negative delays, s=1). This is the raw and unambiguous signal evaluated for quantitative analysis with the kinetic model in Fig. 2 in the main text. **b** Difference RIXS intensities where the subtracted intensities of ground-state $Fe(CO)_5$ were scaled by the given scaling factors s ranging from 0.95 (top) to 0.85 (bottom). Left column: Delay intervals of 0-700 fs. Right column: Delay intervals of 0.7-3.5 ps. **c** For comparison: RIXS intensities of ground-state $Fe(CO)_5$. The scaling factor used in Fig. 1c in the main text is s=0.9.

The remaining $Fe(CO)_5$ ground-state RIXS intensity is smaller at positive delay times compared to negative delay times due to the ground-state bleach concomitant with photo-

excitation. This is accounted for by subtracting from the raw measured intensities at positive delays scaled reference intensities of $Fe(CO)_5$ (scaling factor 0.9) thus removing an arbitrary amount of remaining un-pumped $Fe(CO)_5$. Note that zero scaling (s=1) corresponds to the direct difference of pumped minus unpumped intensities (Fig. 2a in the main text) whereas maximum scaling (s=0) corresponds to the measured raw signal dominated by $Fe(CO)_5$. Ideally, the scaling factor corresponds to the fraction of photo-excited $Fe(CO)_5$ molecules. As this fraction could not be determined from experimental parameters with high enough accuracy to determine the scaling factor independently, we rather investigated RIXS difference intensities with different scaling factors with the aim to determine the approximate scaling factor based on the criterion not to generate negative intensities (too large s) and still subtracting the dominant contribution of ground-state $Fe(CO)_5$. The result is shown in Fig. S2. A scaling of s=0.975 is not enough to compensate for the ground-state bleach whereas at s=0.85 the ground-state intensities at around 711.5 eV start dominating the spectrum. The RIXS intensities for s=0.925-0.875 are qualitatively similar and for the illustrative purposes aimed at here they can be all considered representative for the RIXS intensities of transients at the given time delays. In the main text (Fig. 1c) the scaling factor is s=0.9. Note that due to the remaining ambiguity in the determination of s we deduced any quantitative information solely from the raw measured data as discussed in the main text with Fig. 2.

2. Computational details

Fe L_3-RIXS intensities were derived from restricted active space self-consistent field (RASSCF) calculations as detailed in the following. In addition we give supporting information on the assignments of RIXS intensities within the many-electron total energy picture for $Fe(CO)_5$ and excited-state $Fe(CO)_4$. To scrutinize our calculations we furthermore compare the calculated and measured optical absorption spectra of $Fe(CO)_5$ and verify our calculated RASSCF valence-excited state energies with state-of-the-art calculations. Finally, we detail bonding in $Fe(CO)_5$, $Fe(CO)_4$ and $Fe(CO)_4$-EtOH and the symmetries of the d_σ* and d_π orbitals.

2.a. Details of the restricted active space self-consistent field (RASSCF) calculations

Fe L_3-RIXS intensities were calculated as described in ref. 40 and derived from restricted active space self-consistent field (RASSCF) calculations[41] using the MOLCAS-7 software[42]. Scalar relativistic effects were introduced via the second order Douglas-Kroll-

Hess Hamiltonian[43, 44]. Spin-orbit coupling effects were calculated using the state-interaction technique[45] The TZVP basis sets[46] were used for all atoms except for hydrogen for which we used the DZP basis set.

The active space in the RASSCF calculations included 14 electrons in 14 orbitals. The 2p orbital in the RAS1 space contained at most one hole. Four 3d electrons were placed in the RAS2 space. RAS3 contained seven orbitals including the nominally empty 3d orbital with at most 2 electrons. To ensure convergence in the RASSCF calculations, the 2p orbitals were frozen. The RASSCF calculations were initialized with orbitals adapted to the core-excited and valence-excited states by performing prior SCF calculations with and without a core-hole (distributed over the 2p orbitals) present. State-averaging was done separately over the core-excited and the valence-excited states. The final states and dipole transition moments were obtained through the state-interaction including spin-orbit coupling between the 440 core-excited states and 320 valence-excited states, including the ground state.
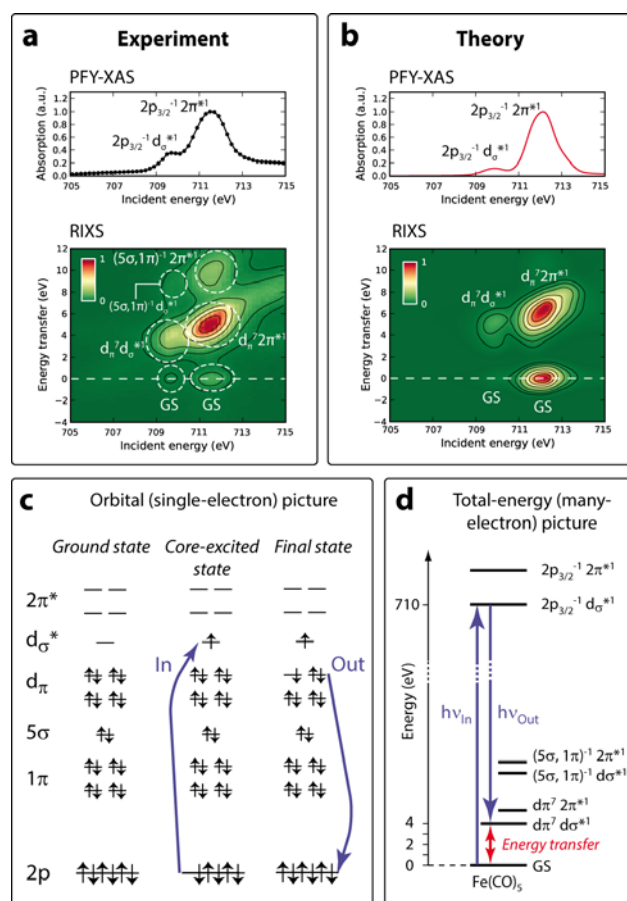
Fe L_3-RIXS intensities were calculated using the Kramers-Heisenberg formula[47]. Spectra were calculated for an ensemble of randomly oriented molecules excited by linearly polarized light and detected in the plane of polarization according to the experimental geometry (see **Experimental Details**). Interference effects were excluded. To account for lifetime broadening in the core-excited states, a Lorentzian broadening of 0.3 eV (FWHM) was used[48]. The RIXS maps were also broadened along the incident-photon energy axis with a Gaussian of 0.5 eV (FWHM) accounting for the SXR monochromator resolution and along the energy-transfer axis with a Gaussian of 1 eV (FWHM) accounting for the resolution of the RIXS spectrometer according to the experimental parameters (see **Experimental Details**). An additional Gaussian broadening of 0.5 eV (FWHM) had to be applied to both axes to best match calculated and measured spectra. We believe that this is due to spectral broadening in the experiment due to a continuum of configurations with slightly different incident energies and energy transfers that is not included in the calculations based on selected configurations. All RIXS calculations employed C_{2v} symmetry, except for the $FeCO_4$-EtOH complexes which had C_s symmetry.

2.b. Assignments within the many-electron total energy picture – Fe L_3-RIXS of Fe(CO)$_5$ and excited-state Fe(CO)$_4$

We assess the quality of our Fe L_3-RIXS calculations and assignments by comparing the measured intensities of Fe(CO)$_5$ with calculated intensities of Fe(CO)$_5$ in an optimized

geometry (Fig. S3 and Fig. 2 in the main text). Our calculations reproduce the $d_\pi \rightarrow d_\sigma*$ and $2p \rightarrow LUMO$ transition energies to within 1 eV. The deficiencies in the calculated spectrum (missing intensity for 10 eV energy transfer and excess intensity at zero energy transfer) do not influence our conclusions (see below).

The ground-state valence-electron configuration of $Fe(CO)_5$ as depicted in Fig. 1 in the main text and as assigned throughout the text is $d_\pi^8 d_\sigma*^0$ ($^1A_1'$) where the antibonding $d_\sigma*$ orbital has a_1' symmetry and the d_π orbitals are composed of the e' and e'' orbitals. By accounting in addition for the lower-lying orbitals, the ground-state electron configuration can also be written as $Fe(CO)_5$ $1\pi^{20} 5\sigma^{10} d_\pi^8 d_\sigma*^0 2\pi*^0$ ($^1A_1'$). Inclusion of the lower-lying orbitals is necessary to assign all features in the Fe L_3-RIXS measurement in Fig. 1 in the main text. This is discussed with Fig. S3 based on a comparison of measured and calculated spectra.

Supplementary Information Figure S3: Measured (**a**) and calculated RASSCF (**b**) Fe L_3-RIXS intensities and partial-fluorescence yield (PFY) x-ray absorption spectra of ground-state $Fe(CO)_5$ with assignments of peaks and illustrations of the assignments in the orbital (single-electron) picture (**c**) and in the total-energy (many electron) picture (**d**). The RIXS intensity is encoded in color (see color bars) and plotted versus energy transfer and incident photon energy. The PFY x-ray absorption spectrum in (**a**) was derived from the RIXS data by plotting the intensities integrated along the energy-transfer axis versus incident photon energy.

The experimental PFY x-ray absorption spectrum (Fig. S3a) exhibits two main peaks. Comparison to the calculated spectrum (Fig. S3b) shows that the pre-edge (main-edge) peak at 709.5 eV (711.5 eV) corresponds to transitions of Fe 2p electrons to the unoccupied $d\sigma*$ ($2\pi*$) orbitals ("In" in Fig. S3c) leading to the $2p_{3/2}^{-1}d\sigma*^1$ [$2p_{3/2}^{-1}2\pi*^1$] core-excited states ("$h\nu_{In}$" in Fig. S3d). Inelastic scattering through these $2p_{3/2}^{-1}d\sigma*^1$ [$2p_{3/2}^{-1}2\pi*^1$] core resonances

("Out" in Fig. S3c, "$h\nu_{Out}$" in Fig. S3d) leads to the final (valence-excited metal-centered ligand-field) states with $d_\pi{}^7 d_\sigma*^1$ [$d_\pi{}^7 2\pi*^1$] configurations at energy transfers of 3-5 eV (4-7 eV). The energy transfer in the inelastic scattering process is calculated as the difference between incident and scattered photon energies. In the one-electron picture (Fig. S3c) the resulting transitions in the final states correspond to $d_\pi \rightarrow d_\sigma*$ and $d_\pi \rightarrow 2\pi*$ single-electron transitions (only the latter is depicted in Fig. S3c).

Scattering back to the ground state corresponds to elastic scattering (zero energy transfer) and is denoted "GS". The intensity maxima in the experimental RIXS data in Fig. S3a are labeled accordingly. The calculated elastic scattering intensities are too strong compered to experiment. This can be explained by experimental factors influencing the measured elastic scattering which are not included in the calculations (surface roughness of the sample, polarization dependence of elastic scattering).

We assign the RIXS features at energy transfers of 9-11 eV (Fig. S3a) to final (valence-excited ligand-centered charge-transfer) states with $(5\sigma,1\pi)^{-1}d_\sigma*^1$ and $(5\sigma,1\pi)^{-1}2\pi*^1$ configurations in agreement with the previously reported Fe L-edge RIXS study of $Fe(CO)_5$ in toluene solution[49]. The 5σ and 1π orbitals are not included in the active space of our RASSCF calculations and, as a consequence, the corresponding intensity maxima are not modeled in the calculated RIXS intensities. The good agreement of RIXS features corresponding to ligand-field states in our calculations to the recently reported RASSCF Fe L-RIXS calculations of $Fe(CO)_5$ including the charge-transfer states in ref. 49 demonstrates that omission of these states does not affect the calculated spectra in the regions of ligand-field states that we focus on here.

RIXS from electronically excited states with negative energy transfers is explained for the excited-state species $Fe(CO)_4$ (E, $^1B_2$) within the orbital (one-electron) and within the total-energy (many-electron) pictures with the calculated Fe L_3-RIXS intensities in Fig. S4.
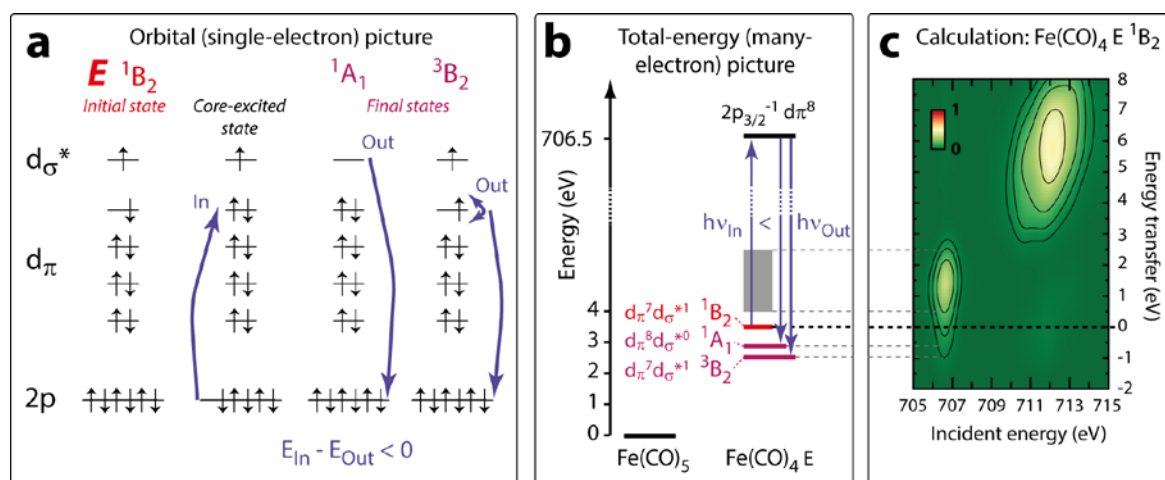
Supplementary Information Figure S4: RIXS from electronic excited states at negative energy transfers. **a** Illustration of the Fe L_3-RIXS assignments in the orbital (single-electron) picture in the total-energy (many electron) picture (**b**) for RIXS at negative energy transfers in the calculated RASSCF RIXS (**c**) from the electronic excited $^1B_2$ state of $Fe(CO)_4$ in E geometry. The relative energies of the $Fe(CO)_4$ states are taken from Fig. S10. The RIXS intensity in **c** is encoded in color (see color bar) and plotted versus energy transfer and incident photon energy. Only those transitions are assigned that result in negative energy transfers.

Pre-edge x-ray absorption in excited $Fe(CO)_4$ ($^1B_2$) at 706.5 e V corresponds to transitions of Fe 2p electrons to the partially unoccupied $d\pi$ orbital ("In" in Fig. S4a) leading to the $2p_{3/2}^{-1}d\pi^1$ core-excited states ("$h\nu_{in}$" in Fig. S4b). Absorption at the main edge at 712 eV is not considered here as it does not lead to negative energy transfers. Inelastic scattering through $2p_{3/2}^{-1}d\pi^1$ can lead to the final ligand-field $d_\pi^8 d_\sigma^0$ ($^1A_1$) state ("Out" in Fig. S4a, "$h\nu_{out}$" in Fig. S4b) located at energy transfers of close to -1 eV (Fig. S4c). In the single-electron picture this corresponds to the $d_\sigma^* \rightarrow d_\pi$ single-electron transition. In the total-energy (many-electron) picture the zero energy transfer line (elastic scattering, dashed line in Fig. S4c) is aligned with the state where the x-ray photon was absorbed, here $^1B_2$, revealing that the transition to $^1A_1$ corresponds to a negative energy transfer. Inelastic scattering through $2p_{3/2}^{-1}d\pi^1$ can in addition lead to the final ligand-field state $d_\pi^7 d_\sigma^1$ ($^3B_2$) at negative energy transfers. In the one-electron picture this corresponds to elastic scattering with additional spin flip (Fig. S4a). The many-electron picture shows that the transition occurs to a lower-lying state hence resulting in negative energy transfer ("$h\nu_{out}$" is not shown for this case in Fig. S4b). Inelastic scattering through $2p_{3/2}^{-1}d\pi^1$ to higher-lying valence-excited states represented by the grey box in Fig. S4b leads to positive transfers extending up to 2.5 eV (Fig. S4c).

2.c. Comparing the calculated and measured optical absorption spectra of Fe(CO)₅

In order to scrutinize our calculational approach we compare in Fig. S5 the calculated RASSCF and measured optical absorption spectrum of $Fe(CO)_5$. The calculated intensities

correspond to the dipole transitions strengths between the ground and the valence excited states (the latter are the final states in RIXS). They were derived from the oscillator strengths of the valence-excitations as obtained from the state-interaction calculations in the MOLCAS-7 software. The satisfying agreement and in particular the correctly reproduced onset of electronic transitions at around 300 nm shows that our RASSCF calculations give a good description of the valence-electronic structure.

Note that with the calculated optical spectrum in Fig. S5 we also confirm the assignments of transitions at our pump-laser wavelength of 266 nm reported in refs. 50 and 51. The calculated transitions in the range covered by the laser-pump radiation of approximately 240-290 nm are dominated by metal to ligand charge transfer (MLCT) excitations with transitions from Fe-centered nominal 3d d_π (e', e'') orbitals to antibonding ligand-centered nominal CO $2\pi*$ (e', e'') orbitals.
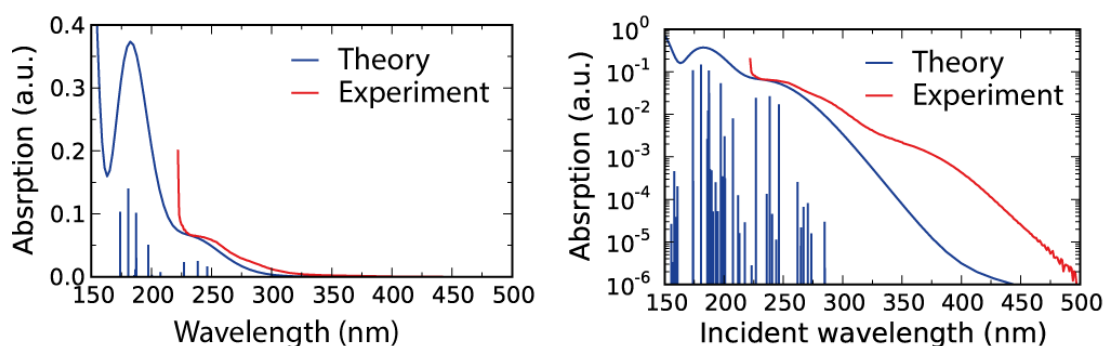
Supplementary Information Figure S5: Calculated RASSCF and measured[52] optical absorption spectrum of $Fe(CO)_5$ (gas phase) with absorption on a linear (left) and logarithmic scale (right). The blue sticks represent calculated single transitions and the solid blue line results from summing all intensities of the sticks convoluted with Gaussian profiles (FWHM 1 eV).

2.d. Verification of the RASSCF valence-excited state energies – Comparison to state-of-the-art

The calculated RASSCF energies of various valence-excited states of $Fe(CO)_5$ and $Fe(CO)_4$ are compared in Tab. S1 to the results of CASSCF and CASPT2 calculations and to published results in ref. 53 and in ref. 54. This shows that the RASSCF calculations agree to within roughly 0.5-1 eV with our CASSCF, CASPT2 and published results based the same methods. This demonstrates that the calculated Fe L_3-RIXS observables can be expected to be affected by a similar amount by the approximations used in the RASSCF calculations and justifies the criterion of matching spectral features to within 1 eV in selecting the species for the kinetic model (see discussion below for how structures were selected in the kinetic model).

Supplementary Information Table S1: Evaluation of the ligand-field valence-excitations from the RASSCF calculations used to derive the calculated Fe L_3-RIXS spectra against results from calculations by us and from the literature aiming only at giving the best possible energies for the valence-excited states. Our SA-CASPT2(12,12) calculations are CASPT2(12,12) calculations are state-averaged over 6 states in each symmetry class in C_{2v} symmetry using the TZVP basis set. Our CASPT2(12,12) calculations are state-specific calculations in C_{2v} symmetry using the TZVP basis set. All energies are in eV and the energy of the ground state of Fe(CO)$_5$ ($^1A_1'$) was set to zero. The calculations of FeCO$_5$ ($^1A_1'$), FeCO$_4$ ($^3B_2$), and FeCO$_4$ ($^1A_1$) were done in the optimized geometries of the respective species and states (for details of structures see Tab. S2).

Method	Ref.	Species and state						
		FeCO$_5$ ($^1A_1'$)	FeCO$_5$ ($^3E'$)	FeCO$_5$ ($^3E''$)	FeCO$_5$ ($^1E'$)	FeCO$_5$ ($^1E''$)	FeCO$_4$ ($^3B_2$)	FeCO$_4$ ($^1A_1$)
RASSCF (Fe L_3-RIXS)	This work	0	3.2	4.1	4.6	5.3	-	-
SA-CASSCF(12,12)	This work	0	3.9	4.6	5.1	5.6	-	-
SA-CASPT2(12,12)	This work	0	3.3	4.0	4.4	4.7	-	-
CASPT2(12,12)	This work	0	3.5	4.2	4.5	4.6	1.7	2.1
CASPT2(10,10)	Ref. 53, Tab. 4	0	3.4	4.2	4.3	5.1	-	-
CASPT2(12,12)	Ref. 54, Tab. 2	0	-	-	-	-	1.9	2.2

2.e. Bonding in Fe(CO)$_5$, Fe(CO)$_4$ and Fe(CO)$_4$-EtOH and symmetries of the $d_\sigma*$ and d_π orbitals

In Figure S6 a simplified molecular-orbital diagram of Fe(CO)$_5$, Fe(CO)$_4$ and Fe(CO)$_4$-EtOH as derived from our calculations is depicted. For simplicity, the molecular orbitals contributing most to the bonding are grouped into 5σ, d_π, $d_\sigma*$ and $2\pi*$ according to their symmetry with respect to the Fe-CO bond and the metal (3d) or ligand (5σ, 2π) character. These are also the labels used throughout the text. In addition, interaction with the CO 1π orbital as according to the allylic model is omitted here for simplicity.
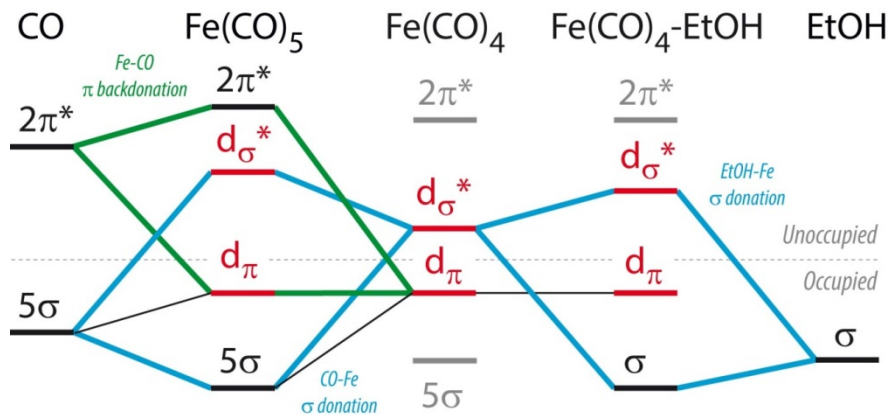
Supplementary Information Figure S6: Orbital interactions of Fe(CO)$_4$. Simplified molecular-orbital diagram depicting bonding of Fe(CO)$_4$ with CO and ethanol with a focus on the Fe-centered d_π and $d_\sigma*$ orbitals (red). The 5σ and $2\pi*$ orbitals are partly omitted for clarity. The energetic splitting of the various d_π orbitals is omitted for clarity as it is small on the energy scale shown here. σ donation (π backdonation) is indicated in blue (green). The dashed line separates occupied and unoccupied orbitals in the electronic ground-states of the respective systems.

3. The kinetic model

Details of the kinetic model including a discussion of how we selected structures for the photoproducts and with details on structures and spectra for the photoproducts are given in the following. The kinetic model discussed in the main text as well as alternative kinetic models are presented. Finally, the potential contribution of $Fe(CO)_3$ as a photoproduct is discussed.

3.a. Selection of structures for the photoproducts

To establish a systematic correlation between geometry, chemical bonding and Fe L_3-RIXS intensities, we calculated spectra of a total of 70 s tructures including ground- and excited states of $Fe(CO)_5$ and possible photofragment species of $Fe(CO)_4$ and complexes of $Fe(CO)_4$ with solvent molecules. Structures were selected based on matching the measured RIXS intensity differences in Fig. 2a in the main text and were taken into account if they agreed with experiment in incident photon energy and energy transfer to within 1 eV or less (the uncertainty in reproducing the absolute energy of measured spectral features, see above).

To test the robustness of our assignments and to approximate the time evolution of the structures by accounting for structural averaging resulting from sampling of various geometries in the system, we calculated spectra of different geometries for each electronic state. Three geometries were calculated for each of the three non-complexed states (excited-state singlet, triplet and singlet), three were calculated for "hot" $Fe(CO)_5$ and two geometries were calculated for the solvent-complexed species. The photofragment spectra used in Fig. 2b in the main text thus result from a total of 14 geometries.

3.b. Details on structures and spectra for the photoproducts

The three calculated geometries for each of the three non-complexed species are denoted $Fe(CO)_4$ E, $Fe(CO)_4$ T and $Fe(CO)_4$ S and they were obtained by optimizing the geometry of $Fe(CO)_4$ in C_{2v} symmetry with CASPT2 in the lowest singlet B_2 state, in the lowest triplet state and in the lowest singlet state, respectively. The geometries and the corresponding Fe L_3-RIXS intensities are shown in Figure S7.

The three calculated geometries for "hot" $Fe(CO)_5$ are denoted $Fe(CO)_5$ $C_{2v}90$, $Fe(CO)_5$ $C_{4v}120$, and $Fe(CO)_5$ $C_{4v}180$. They were obtained by manually changing angles compared to the optimized geometry and are shown with the corresponding Fe L_3-RIXS intensities in Figure S8.

The two calculated geometries for the solvent-complexed $Fe(CO)_4$-EtOH species are denoted $Fe(CO)_4$-EtOH B and $Fe(CO)_4$-EtOH C and they were obtained by optimizing with CASPT2 and DFT-PBE, respectively, the geometry of $Fe(CO)_4$-EtOH in C_s symmetry in the lowest singlet state. In $Fe(CO)_4$-EtOH B, $Fe(CO)_4$ and ethanol interact via the hydroxyl group of ethanol whereas in $Fe(CO)_4$-EtOH C the interaction is via the alkyl group. Their geometries and Fe L_3-RIXS intensities are shown in Figure S9.

Details on symmetries, bond distances and angles and a comparison to previously reported structures for all 14 geometries are given in Table S2.
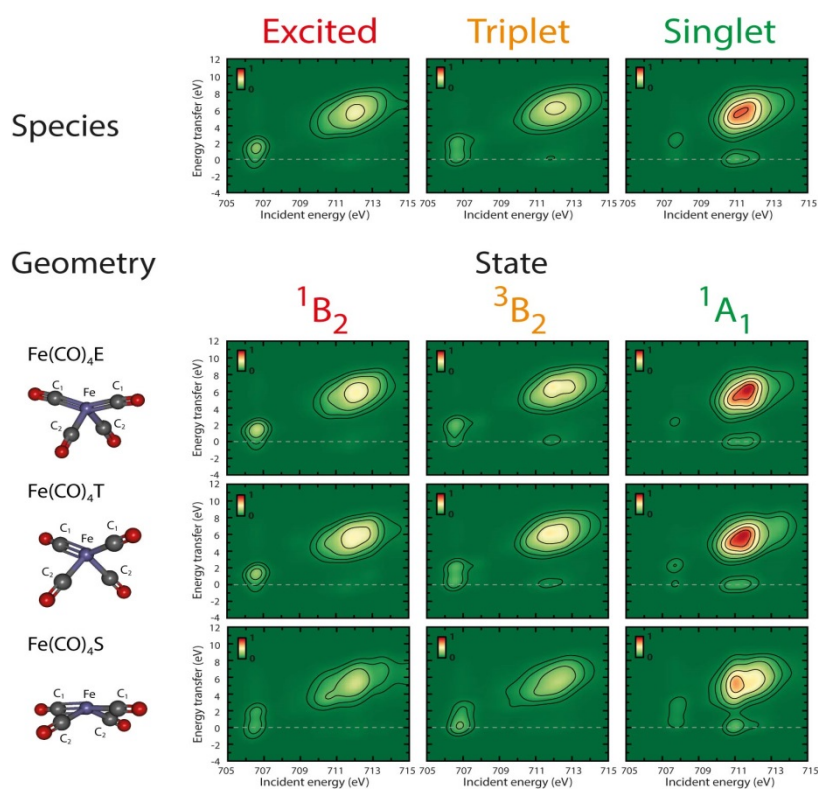
Supplementary Information Figure S7: Calculated Fe L_3-RIXS intensities of the non-complexed $Fe(CO)_4$ species. According to their electronic structure these are: Excited singlet-state ($d\pi^7 d\sigma^{*1}$, $^1B_2$), triplet ($d\pi^7 d\sigma^{*1}$, $^3B_2$) and singlet ($d\pi^8 d\sigma^{*0}$, $^1A_1$) $Fe(CO)_4$. The intensities of each species is the sum of three contributions for the same ligand coordination and electronic state but three different geometries denoted $Fe(CO)_4$ E, $Fe(CO)_4$ T and $Fe(CO)_4$ S (calculated geometries are depicted on the left, for details on distances and angles see Table S2). Intensities are encoded in color (see color bar). In contrast to Fig. 2b in the main text, were intensities are normalized to 1 at the maximum, the intensities are plotted here as calculated and as used in the kinetic model not to influence the derived populations by the intensity normalization.
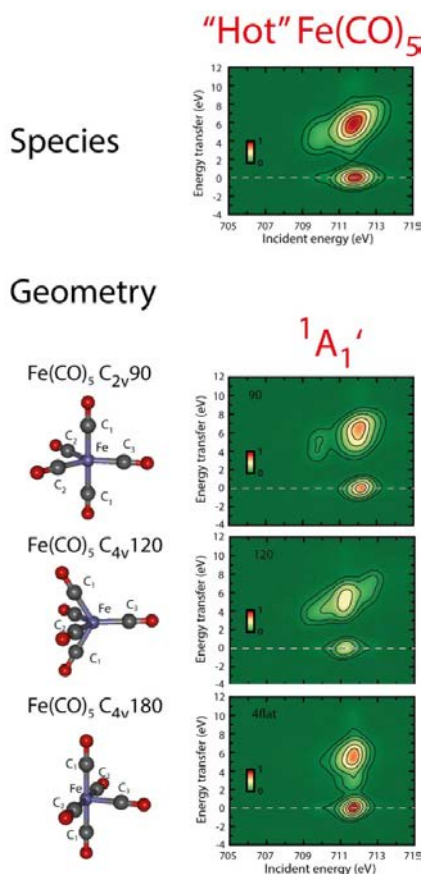
Supplementary Information Figure S8: Calculated Fe L_3-RIXS intensities of the "hot" $Fe(CO)_5$ species. T hese are represented by three geometries (calculated structures are depicted on the left, for details on distances and angles see Table S2) ($d\pi^8 d\sigma^{*0}$, $^1A_1'$). Intensities are encoded in color (see color bar). In contrast to Fig. 2b in the main text, were intensities are normalized to 1 at the maximum, the intensities are plotted here as calculated and as used in the kinetic model not to influence the derived populations by the intensity normalization
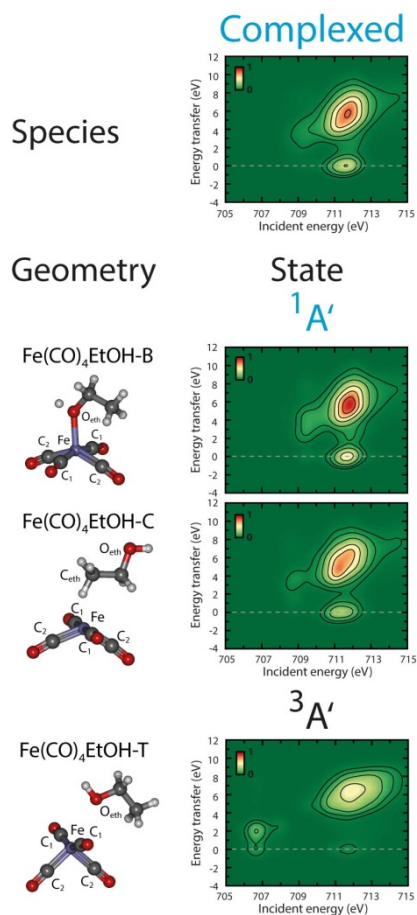
Supplementary Information Figure S9: Calculated Fe L_3-RIXS intensities of the complexed $Fe(CO)_4$ species. These are solvent-complexed structures $Fe(CO)_4$-EtOH ($d\pi^8 d\sigma^{*0}$, $^1A'$) with the two calculations shown below for the same ligand coordination and electronic state but two different geometries denoted $Fe(CO)_4$-EtOH-B and $Fe(CO)_4$-EtOH-C (calculated geometries are depicted on the left, for details on distances and angles see Table S2). Bonding of ethanol to $Fe(CO)_4$ is via the ethanol hydroxyl group in $Fe(CO)_4$-EtOH-B and via the ethanol alkyl group in $Fe(CO)_4$-EtOH-C. Intensities are encoded in color (see color bar). In contrast to Fig. 2b in the main text, were intensities are normalized to 1 at the maximum, the intensities are plotted here as calculated and as used in the kinetic model not to influence the derived populations by the intensity normalization. For comparison, the calculated RIXS intensities of the non-interacting configuration of triplet $Fe(CO)_4$ ($^3B_2$, $d\pi^7 d\sigma^{*1}$) with ethanol close by [$Fe(CO)_4$-EtOH-T, $^3A'$ and $d\pi^7 d\sigma^{*1}$] is shown.

Supplementary Information Table S2: Symmetries, distances, and angles for the calculated geometries as compared to previously reported structures. For the assignments C_1, C_2, O_{eth} and C_{eth} see the plotted structures in Figures S7-S9.

| Geometry	Symmetry	Distances	Angles	Notes
$Fe(CO)_5$	D_{3h}	$d(Fe-C_{eq}) = 1.80$ Å $d(Fe-C_{ax}) = 1.81$ Å $d(C-O) = 1.15$ Å		Optimized with CASPT2 in the lowest singlet state (ground state) in C_{2v} symmetry.
$Fe(CO)_5$ $C_{2v}90$	C_{2v}	$d(Fe-C_1) = 1.81$ Å $d(Fe-C_2) = 1.80$ Å	$<(C_1-Fe-C_1) = 180.0°$ $<(C_2-Fe-C_2) = 90.0°$ $<(C_1-Fe-C_3) = 90.0°$	Fixed geometry (without optimization)
$Fe(CO)_5$ $C_{4v}120$	C_{4v}	$d(Fe-C_1) = 1.81$ Å $d(Fe-C_2) = 1.80$ Å $d(Fe-C_3) = 1.81$ Å	$<(C_1-Fe-C_1) = 120.0°$ $<(C_2-Fe-C_2) = 120.0°$ $<(C_1-Fe-C_3) = 120.0°$	Fixed geometry (without optimization). Calculation made in C_{2v} symmetry.
$Fe(CO)_5$ $C_{4v}180$	C_{4v}	$d(Fe-C_1) = 1.80$ Å $d(Fe-C_2) = 1.80$ Å $d(Fe-C_3) = 1.81$ Å	$<(C_1-Fe-C_1) = 180.0°$ $<(C_2-Fe-C_2) = 180.0°$ $<(C_1-Fe-C_3) = 90.0°$	Fixed geometry (without optimization). Calculation made in C_{2v} symmetry.
$Fe(CO)_4 T$	C_{2v}	$d(Fe-C_1) = 1.87$ Å $d(Fe-C_2) = 1.84$ Å	$<(C_1-Fe-C_1) = 148.1°$ $<(C_2-Fe-C_2) = 97.3°$	Optimized with CASPT2 in the lowest triplet state (ground state) in C_{2v} symmetry.
$Fe(CO)_4 S$	C_{2v}	$d(Fe-C_1) = 1.82$ Å $d(Fe-C_2) = 1.79$ Å	$<(C_1-Fe-C_1) = 182.5°$ $<(C_2-Fe-C_2) = 139.1°$	Optimized with CASPT2 in the lowest singlet state in C_{2v} symmetry.
$Fe(CO)_4 E$	C_{2v}	$d(Fe-C_1) = 1.86$ Å $d(Fe-C_2) = 1.80$ Å	$<(C_1-Fe-C_1) = 152.5°$ $<(C_2-Fe-C_2) = 97.8°$	Optimized with CASPT2 in the lowest singlet B_2 state in C_{2v} symmetry.
$Fe(CO)_4$- EtOH-B	C_s	$d(Fe-C_1) = 1.80$ Å $d(Fe-C_2) = 1.79$ Å $d(Fe-O_{eth}) = 2.13$ Å	$<(C_1-Fe-C_1) = 198.2°$ $<(C_2-Fe-C_2) = 136.9°$	Optimized with CASPT2 in the lowest singlet state (ground state) in C_s symmetry. Ethanol binds with the hydroxyl group.
$Fe(CO)_4$- EtOH-C	C_s	$d(Fe-C_{eth}) = 2.89$ Å $d(Fe-O_{eth}) = 4.80$ Å	$<(C_1-Fe-C_1) = 181.5°$ $<(C_2-Fe-C_2) = 126.9°$	Optimized with DFT-PBE in the lowest singlet state (ground state) in C_s symmetry. Ethanol binds with the alkyl group.
$Fe(CO)_4$- EtOH-T	C_s	$d(Fe-O_{eth}) = 3.01$ Å $d(Fe-C_1) = 1.85$ Å $d(Fe-C_2) = 1.80$ Å	$<(C_1-Fe-C_1) = 151.9°$ $<(C_2-Fe-C_2) = 96.9°$	Optimized with DFT-PBE in the lowest triplet state in C_s symmetry. Ethanol binds with the hydroxyl group.
Previously reported structures				
$Fe(CO)_4 {}^1A_1$	C_{2v}	$d(Fe-C_1) = 1.81\pm 0.03$Å $d(Fe-C_2) = 1.77\pm 0.03$Å	$<(C_1-Fe-C_1) = 169\pm2°$ $<(C_2-Fe-C_2) = 125\pm2°$	Ihee, Zewail and co-workers, Angew. Chem. Int. Ed. **40**, 1532-1536 (2001), ref. 18 in the main text.
$Fe(CO)_4 {}^3B_2$	C_{2v}	$d(Fe-C_1) = 1.87$ Å $d(Fe-C_2) = 1.85$ Å	$<(C_1-Fe-C_1) = 146°$ $<(C_2-Fe-C_2) = 99°$	Snee et al., JACS 123, 2255-2264 (2001), ref. 19 in the main text.
$Fe(CO)_4 {}^3B_2$	C_{2v}	$d(Fe-C_1) = 1.88$ Å $d(Fe-C_2) = 1.86$ Å	$<(C_1-Fe-C_1) = 147.6°$ $<(C_2-Fe-C_2) = 98.3°$	B3LYP in Gonzalez-Blanco et al., J. Chem. Phys. **110**, 778-783 (1999), ref. 55.
$Fe(CO)_4 {}^1A_1$	C_{2v}	$d(Fe-C_1) = 1.83$ Å $d(Fe-C_2) = 1.80$ Å	$<(C_1-Fe-C_1) = 154.0°$ $<(C_2-Fe-C_2) = 133.9°$	B3LYP in Gonzalez-Blanco et al., J. Chem. Phys. 110, 778-783 (1999) ref. 55.

Comparing the calculated spectra in Figs. S7-S9 we find that geometrical changes that preserve ligand coordination and electronic state minimally influence the Fe L_3-RIXS spectra (0.1 eV level) a posteriori justifying our limited set of structures. This means in particular that we cannot distinguish different structures for a given ligand coordination and electronic state. In particular, we cannot determine bond angles in both singlet and triplet $Fe(CO)_4$. Also, coordinative saturation of $Fe(CO)_4$ by ligation with CO or ethanol cannot be distinguished as the calculated spectra of $Fe(CO)_5$ in distorted geometries and of $Fe(CO)_4$-EtOH are very similar when probed with the spectral resolution used here. This also means we cannot determine how in detail ethanol coordinates to $Fe(CO)_4$. It also shows that we are not sensitive to the postulated weak complex formation of $Fe(CO)_5$ in ethanol solution[56] as the

associated structural changes affect the electronic structure as probed with Fe L-edge RIXS to a minor degree only.

Our calculated geometries of the $Fe(CO)_4$ photoproducts compare well with previously reported structures (Table S2). For singlet $Fe(CO)_4$ ($^1A_1$) in $Fe(CO)_4$ S geometry our calculated distances agree, within experimental uncertainties, with the measured distances reported by Ihee , Zewail and co-workers[16].Their angles lie in between our calculated angles of singlet and triplet $Fe(CO)_4$ in $Fe(CO)_4$ S and $Fe(CO)_4$ T geometries. This does not influence our conclusions as we are mainly sensitive to the ligand coordination and electronic state (electronic structure in contrast to geometric structure) as demonstrated with Figure S7 where we show that the spectra of triplet $Fe(CO)_4$ ($^3B_2$) are very similar for the two geometries mentioned above with different angles. The structure of triplet $Fe(CO)_4$ ($^3B_2$) is identical to within 1-2% with the structure reported by Snee et al.[19] and the B3LYP results by González-Blanco et al.[55]. For singlet $Fe(CO)_4$ ($^1A_1$) our optimized bond distances are in very good agreement (within 1-2%) with the B3LYP results by González-Blanco et al.[55] while our angles deviate. We note that our choice of CASPT2(12,12) is the state of the art and that our spectra are insensitive anyway to this angular deviation.

In Figure S9 we also show the calculated Fe L_3-RIXS intensities and geometry of the non-interacting configuration of the $Fe(CO)_4$ triplet species ($^3B_2$) with ethanol close by [$Fe(CO)_4$-EtOH-T ($^3A'$, $d\pi^7 d\sigma^{*1}$)]. Apparently, the RIXS data show only minor differences compared to the RIXS data of triplet $Fe(CO)_4$ without ethanol close by. As can be seen from Table S2, the Fe-O_{eth} distance is larger by 1 Å in $Fe(CO)_4$-EtOH-T compared to the interacting complexes $Fe(CO)_4$-EtOH-B and $Fe(CO)_4$-EtOH-C due to the missing attractive interaction in $Fe(CO)_4$-EtOH-T. This demonstrates that Fe L_3-RIXS directly reflects the bonding of $Fe(CO)_4$ with ethanol (ligand coordination and electronic state) through the concomitant frontier-orbital interactions (Figure S6).

The calculated relative energies of all structures are compared in Figure S10. The association energy (not considering the zero-point energy) of ethanol to $FeCO_4$ ($^1A_1$) is thus calculated to 0.7 (0.2) eV for hydroxyl (alkyl) complexation. These values are consistent with the CCSD(T)/VTP result of 0.33 eV (including zero-point energy) for the association energy of CH_4 to $FeCO_4$ ($^1A_1$)[57].
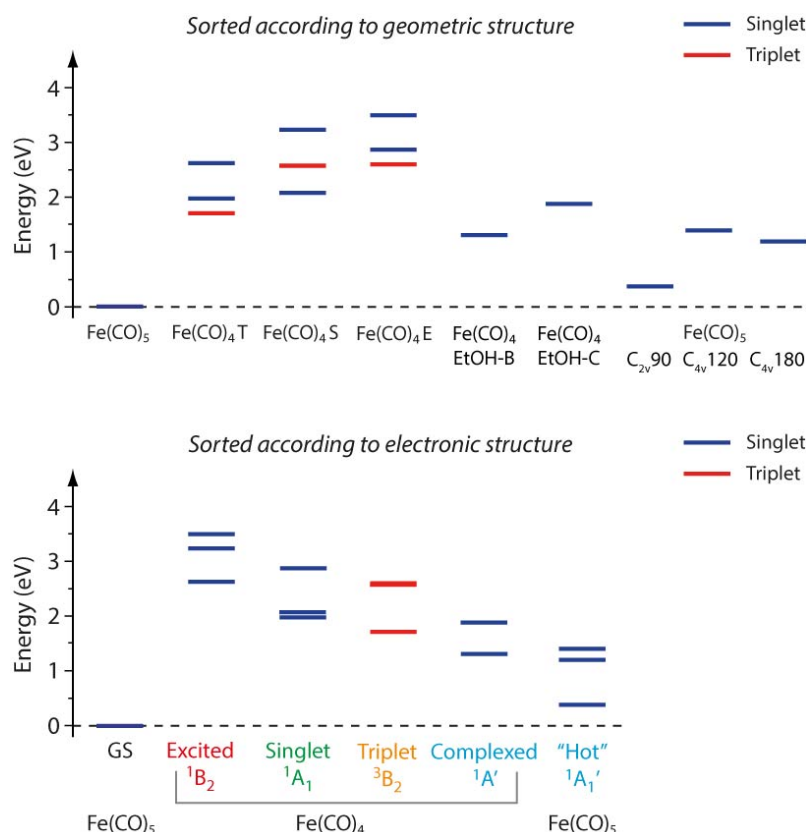
Supplementary Information Figure S10: Calculated relative energies of the calculated structures. Energies are plotted with respect to the ground-state energy of $Fe(CO)_5$ set to zero. Ground states were calculated at the CASPT2 level and excited states result from the RASSCF calculations. For the formation energies of the $Fe(CO)_4$ species and the solvent adduct, we used CASPT2/TZVP calculations on ethanol and CO with active spaces of 14 electrons in 13 orbitals (ethanol) and 8 electrons in 10 orbitals (CO). For the "hot" $Fe(CO)_5$ species we used CASPT2/TZVP calculations on CO with active spaces of 12 electrons in 12 orbitals. Blue: Singlet states, red: triplet states. The energies are sorted according to geometric structure (top) or according to electronic structure (bottom).

3.c. The kinetic model discussed in the main text

The fit in Fig. 2 of the main text is based on a kinetic model with the following rate equations and the excited (E), triplet (T) and ligated (L) $Fe(CO)_4$ species [L denoting "hot" $Fe(CO)_5$ and EtOH-complexed $Fe(CO)_4$-EtOH]:

$$
\begin{cases}
\dfrac{dN_E(t)}{dt} = -\dfrac{1}{\tau_{E \to T}} N_E(t) - \dfrac{1}{\tau_{E \to L}} N_E(t) \\[2em]
\dfrac{dN_T(t)}{dt} = \dfrac{1}{\tau_{E \to T}} N_E(t) \\[2em]
\dfrac{dN_L(t)}{dt} = \dfrac{1}{\tau_{E \to L}} N_E(t)
\end{cases}
\qquad \text{Equations (1)}
$$

Note that the reaction back to excited $Fe(CO)_4$ (E) is not considered as we consider it very unlikely. N(t) denote the populations as a function of time t [$N_E(t)$, e.g., is the population of excited $Fe(CO)_4$] and τ are the time constants characterizing the dynamics of the related populations. $\tau_{E \to T}$, e.g., denotes the time constant for conversion of excited to triplet $Fe(CO)_4$. The rise times $\tau_{E \to T}$ and $\tau_{E \to L}$ are given in Fig. 3 in the main text.

The pump-probe time delay Δt in the experiment corresponds to t in Eqs. (1) as $\Delta t = 0$ corresponds to t=0. N_G denotes the population of ground-state $Fe(CO)_5$ and it was modeled as a reversed Heaviside step function.

The populations N were submitted to the following boundary conditions:

$$
\begin{cases}
N_G(t < 0) = N_G^0 \\
N_G(t \geq 0) = N_G^0 - N_G^{exc} \\
N_E(t < 0) = 0 \\
N_E(t = 0) = N_G^{exc} \\
N_T(t \leq 0) = 0 \\
N_L(t \leq 0) = 0
\end{cases}
\qquad \text{Equations (2)}
$$

where N_G^0 is the concentration of $Fe(CO)_5$ before pumping and N_G^{exc} is the concentration of photoexcited $Fe(CO)_5$ molecules.

The solutions to Eqs. (1) can be written as:

$$
N_G(t \geq 0) = N_G^0 - N_G^{exc}
$$

$$
N_E(t \geq 0) = N_G^{exc} \exp\left[-\left(\frac{1}{\tau_{E \to T}} + \frac{1}{\tau_{E \to L}}\right)t\right]
$$

$$
N_T(t \geq 0) = \frac{\tau_{E \to L}}{\tau_{E \to T} + \tau_{E \to L}} N_G^{exc} \left\{1 - \exp\left[-\left(\frac{1}{\tau_{E \to T}} + \frac{1}{\tau_{E \to L}}\right)t\right]\right\} \qquad \text{Equations (3)}
$$

$$
N_L(t \geq 0) = \frac{\tau_{E \to T}}{\tau_{E \to T} + \tau_{E \to L}} N_G^{exc} \left\{1 - \exp\left[-\left(\frac{1}{\tau_{E \to T}} + \frac{1}{\tau_{E \to L}}\right)t\right]\right\}
$$

The aim of fitting the experimental data with the kinetic model is to determine the quantities $N_E(t)$, $N_T(t)$ and $N_L(t)$ thereby quantifying the population dynamics of the corresponding photo-fragment species. The model was fit to the measured Fe L_3-RIXS intensity differences (integrated intensities of all positive pump-probe delays minus integrated intensities of all negative delays, Fig. 2a in the main text) in 5 energy transfer/incident photon energy regions simultaneously. Only four of these are discussed in the main text with Fig. 2a

and the remaining region is discussed below. See Fig. 2a of the main text for a definition of regions 1-4 and Fig. S11 for the definition of all 5 regions.

The measured RIXS intensity differences I^{dif}_{Ri} (t) versus delay time in a given region R_i can be expressed with Eqs. 3 as

$$I^{dif}_{Ri}(t) = I_{E@Ri}(P * N_E)(t) + I_{T@Ri}(P * N_T)(t) + I_{L@Ri}(P * N_L)(t) + I_{G@Ri}(P * N_G)(t) - I_{G@Ri}N^0_G$$

<div align="right">Equation (4)</div>

where the function P is detailed below and the parameters $I_{G@Ri}$, $I_{E@Ri}$, $I_{T@Ri}$, $I_{L@Ri}$ correspond to the relative RIXS intensities of the respective species in region R_i. These parameters equal the integrated calculated Fe L_3-RIXS intensities of the respective species in region R_i. The calculated RIXS intensities of excited, triplet and complexed $Fe(CO)_4$ and the regions R_i with i=1,…, 5 are depicted in Fig. S12.
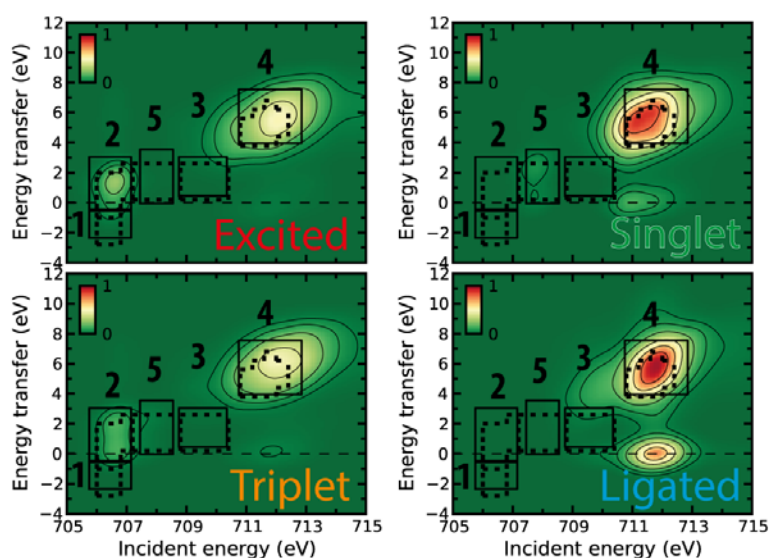
Supplementary Information Figure S11: Calculated RASSCF Fe L_3-RIXS intensities of excited, singlet, triplet, and ligated $Fe(CO)_4$ and definition of the five regions R_i (i=1,…,5) depicted by the boxes with thin solid lines. The intensities are encoded in color (see color bars) and plotted versus energy transfer and incident photon energy. For comparison, the boxes with dashed lines mark the regions used to extract the experimental delay scans (measured intensities versus pump-probe delay time). The experimental boxes were chosen to optimize signal to noise ratios of the respective experimental delay scans while the theoretical boxes were chosen to maximally overlap with the experimental boxes while, as uniquely as possible, identifying the respective species.

The resulting calculated relative intensities $I_{G@Ri}$, $I_{E@Ri}$, $I_{T@Ri}$, $I_{L@Ri}$ (i=1,…,5) are given in Tab. S3. Note that all species approximately equally contribute in region i=4 which hence includes an intensity increase due to the increasing population of reaction intermediates and an intensity decrease due to the $Fe(CO)_5$ ground-state bleach.

Supplementary Information Table S3: Relative intensity parameters $I_{G@Ri}$, $I_{E@Ri}$, $I_{T@Ri}$, $I_{L@Ri}$ (i=1,…,5) of ground-state $Fe(CO)_5$ (G), and the excited (E), triplet (T), and ligated (L) $Fe(CO)_4$ ["hot" $Fe(CO)_5$ and $Fe(CO)_4$-EtOH] in the respective energy transfer/incident photon energy regions i=1,…,5 as defined in Fig. S11. These values were used as input to the kinetic model for identifying the populations of the respective species. All intensities are normalized with respect to the calculated intensity of excited $Fe(CO)_4$ in region 2.

Parameter	Region				
	i=1	i=2	i=3	i=4	i=5
$I_{G@Ri}$	0	0.01	0.15	5.19	0.02
$I_{E@Ri}$	0.24	1.00	0.16	2.93	0.09
$I_{T@Ri}$	0	0.88	0.11	2.93	0.25
$I_{L@Ri}$	0	0.01	0.31	4.88	0.07

The parameters $I_{G@Ri}$, $I_{E@Ri}$, $I_{T@Ri}$, $I_{L@Ri}$ (i=1,…,5) were kept fixed during the fit.

P in Eq. 4 is a function representing the overall temporal resolution of the experiment of 300 fs (FWHM, see **Experimental Details**):

$$P(t) = \frac{2\sqrt{\ln 2}}{FWHM\sqrt{\pi}} \exp\left(-4\ln 2 \frac{(t-t_0)^2}{FWHM^2}\right)$$

Equation (5)

where the pump-probe time delay $\Delta t = 0$ corresponds to $t = t_0$.

Finally, the measured RIXS intensity differences versus pump-probe delay time (delay scans) are fitted simultaneously with the expressions $I_{Ri}(t)$ with i=1,…,5 from Eqs. 6 using the expressions $I^{dif}_{Ri}(t)$ from Eq. 4:

$$\begin{cases} I_{R_1}(t) = a \times a_{R_1} \times I^{dif}_{R_1}(t) + b \\ I_{R_2}(t) = a \times a_{R_2} \times I^{dif}_{R_2}(t) + b \\ I_{R_3}(t) = a \times a_{R_3} \times I^{dif}_{R_3}(t) + b \\ I_{R_4}(t) = a \times a_{R_4} \times I^{dif}_{R_4}(t) + b \\ I_{R_5}(t) = a \times a_{R_5} \times I^{dif}_{R_5}(t) + b \end{cases}$$

Equations (6)

In Eqs. 6 we used an additional global scaling constant a and an additive parameter b and we also explicitly defined the additional scaling constants a_{Ri}, i=1,…,5 for each region. These scaling constants were kept fixed during the fit and they were used to account for the varying pump-laser pulse energies applied in the different regions arising from experimental instabilities over the extended accumulation time. As an exception, the constant a_{R1} was left

free during fitting. This was necessary because the relative intensities of the $(2p_{3/2})^{-1}(d_\sigma^*)^1$ and $(2p_{3/2})^{-1}(2\pi^*)^1$ resonances were not correctly reproduced by the calculations (see Fig S4). Note that the global scaling constant a also accounts for the unknown pump-laser excitation efficiency.

The values $I_{Ri}(t)$ in Eqs. 6 resulting from the fit to the experimental data are plotted as violet lines for regions R_1, R_2 and R_3 in Fig. 2c in the main text and for all regions R_1-R_5 in Fig. S12. The resulting populations $N_E(t)$, $N_T(t)$ and $N_L(t)$ are plotted in Fig. 2c in the main text and in Fig. S12 also including ground-state $Fe(CO)_5$ with population $N_G(t)$. In addition, we plot in Fig. S12 the contributions of the various species to the fitted difference intensities in the various regions [namely the values $I_{E@Ri}(P^*N_E)(t)$, $I_{T@Ri}(P^*N_T)(t)$, $I_{L@Ri}(P^*N_L)(t)$ and $I_{G@Ri}(P^*N_G)(t)$, see Eq. 4].
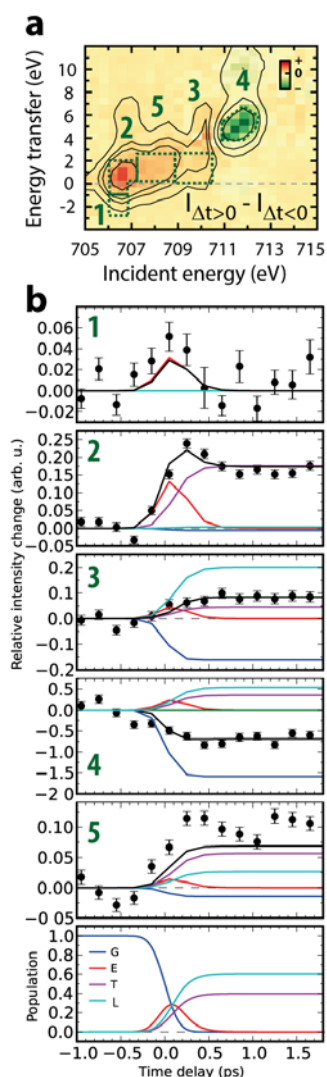

Supplementary Information Figure S12: Contribution of the various species to the delay scans according to the fit of the kinetic model. **a** Measured difference RIXS intensities (integrated intensities of all positive pump-probe delays minus integrated intensities of all negative delays) with energy transfer/incident photon energy regions 1-5, R_i with i=1,…,5 (same plot as in Fig. 2a of the main text except for definition of the additional region 5). The RIXS intensities are encoded in color (see color bars) and plotted versus energy transfer and incident photon energy. **b** Delay scans (experiment: solid circles with error bars, error bars correspond to twice the standard deviation) extracted from the measured intensities integrated in the regions 1-5. Solid black lines in 1-5 are the fitted delay scans based on the kinetic model [$I_{Ri}(t)$ in Eqs. 6]. The contributions of excited (E), triplet (T) and ligated (L) $Fe(CO)_4$ and of ground-state $Fe(CO)_5$ (G) to the fitted difference intensities in the various regions [namely the values of $I_{E@Ri}(P^*N_E)(t)$, $I_{T@Ri}(P^*N_T)(t)$, $I_{L@Ri}(P^*N_L)(t)$ and $I_{G@Ri}(P^*N_G)(t)$, see Eq. 4] are shown in the different delay scans 1-5 as solid lines with colors as indicated. The corresponding populations $N_E(t)$, $N_T(t)$, $N_L(t)$ and $N_G(t)$ are plotted in the bottom panel.

First, this shows that region 1 is by far dominated by excited $Fe(CO)_4$. This establishes with certainty (within the approximations of our calculated Fe L_3-RIXS intensities) the

occurrence of excited $Fe(CO)_4$ as none of the other species contributes to this region in the RIXS map. In fact, other excited-state species of both $Fe(CO)_4$ and $Fe(CO)_5$ were considered but none other was found to fit the measured RIXS data in terms of both incident photon energy and energy transfer.

Second, the comparison in Fig. S12 shows that region 2 i s dominated by the contributions of excited and triplet $Fe(CO)_4$. Region 3 i s dominated by ligated $Fe(CO)_4$ increasing with time and the ground-state bleach of $Fe(CO)_5$ depleting with time. Region 4 is dominated by the ground-state bleach of $Fe(CO)_5$. Region 5 i s dominated by triplet and ligated $Fe(CO)_4$.
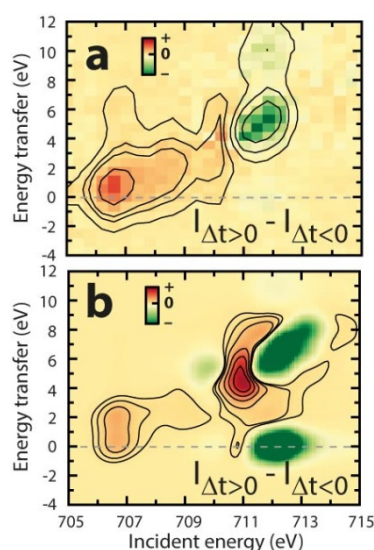

Extended Data Figure 13: Comparison of measured and fitted RIXS intensity differences. The measured (**a**) and fitted (**b**) RIXS intensity differences (integrated intensities of all positive pump-probe delays minus integrated intensities of all negative delays) are encoded in color (see color bars). The measured data are the same as in Fig. 2a of the main text. The agreement is particularly good for incident photon energies of below 711 eV that we primarily focus on in our investigation. Measured differences at 707 eV/7 eV and 712 eV/10 eV are not reproduced because the calculated RIXS intensities do not include charge-transfer states contributing to these regions.

The fitted RIXS intensity differences versus delay time from the kinetic model were used to calculate the fitted RIXS intensity differences as plotted for the experiment (Fig. 2b in the main text). The comparison of fit and experiment is shown in Figure S13.

3.d. Alternative kinetic models

Analysis of kinetic models that included non-complexed singlet $Fe(CO)_4$ ($^1A_1$) are consistent with the experimental data but show these photofragments do not make a statistically significant contribution to the transient difference spectra. The equally good fit in Figure S14a and S14b for models without and with singlet $Fe(CO)_4$ ($^1A_1$), respectively, demonstrates that our data is not sensitive enough to clearly distinguish between a model with or without singlet $Fe(CO)_4$ ($^1A_1$). This is mostly due to the fact that the contribution of singlet $Fe(CO)_4$ to the Fe L_3-RIXS data is comparably weak, that the corresponding spectral region overlaps strongly with contributions of triplet and ligated $Fe(CO)_4$, and that singlet $Fe(CO)_4$ occurs, if at all, as a transient species only. For the sake of simplicity and to focus on the most

valid conclusions from our data we decided to discuss in the main text the model without singlet $Fe(CO)_4$.
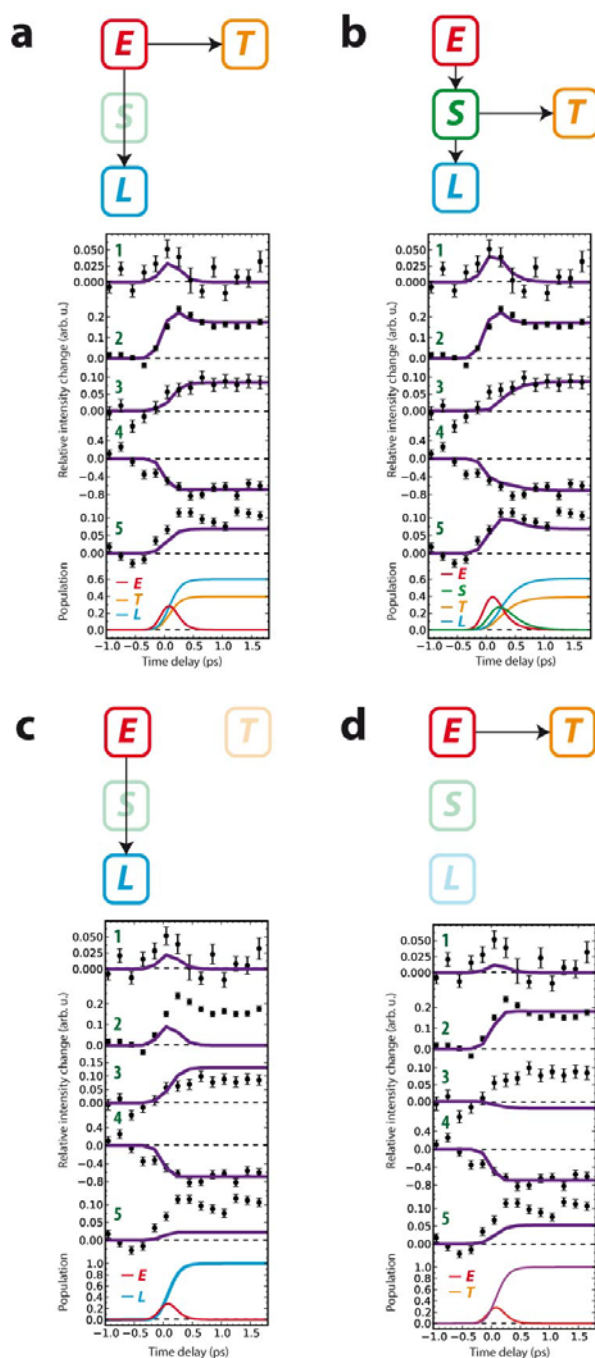
Supplementary Information Figure S14: Alternative kinetic models. Schematic depiction of pathways for alternatives **a-d** of the kinetic model and corresponding fits to the measured data with excited (E), triplet (T), singlet (S) and ligated (L) $Fe(CO)_4$. **a** Model shown and discussed in the main text. **b** Additionally including singlet $Fe(CO)_4$ ($^1A_1$). **c** Excluding triplet ($^3B_2$) and singlet $Fe(CO)_4$. **d** Excluding ligated "hot" $Fe(CO)_5$ and solvent-complexed $Fe(CO)_4$-EtOH. Solid violet lines in 1-5 are the fitted delay scans with the corresponding experimental delay scans (solid circles with error bars, error bars correspond to twice the standard deviation) extracted from the intensities integrated in regions 1-5. The populations of excited (E), triplet (T), singlet (S) and ligated (L) $Fe(CO)_4$ are plotted in the bottom panels as solid lines.

The model including only excited and ligated $Fe(CO)_4$ but excluding triplet and singlet $Fe(CO)_4$ (dashed curve in Fig. 2c, region 2, in the main text) and the model including only triplet $Fe(CO)_4$ but excluding singlet and ligated $Fe(CO)_4$ (dashed curve in Fig. 2c, region 3, in the main text) are shown for all regions in Figure S14c and S14d, respectively. For the latter and in contrast to the experiment, the global fit forces the intensity in region 3 to below zero due to the dominant depletion in the nearby region 4. The model excluding triplet

$Fe(CO)_4$ does not reproduce the measured delay scans of region 2 where triplet $Fe(CO)_4$ dominates. Likewise, the model excluding ligated $Fe(CO)_4$ does not reproduce the measured delay scans of region 3 where ligated $Fe(CO)_4$ dominates. This shows that our data is good enough to distinguish the models with and without triplet and ligated $Fe(CO)_4$ and that we establish with certainty (within the approximations of our calculated Fe L_3-RIXS intensities) the occurrence of triplet and ligated $Fe(CO)_4$.

3.e. On the contribution of Fe(CO)₃ as a photoproduct

$Fe(CO)_3$ has been reported as a possible photoproduct upon single-photon excitation of $Fe(CO)_5$ at 266 nm in solution (ref. 25 of the main text and ref. 58). The yield in heptane solution with respect to $Fe(CO)_4$ was reported for long time delays of 10-20 ps after pumping to vary between 1:17 (ref. 25 of the main text) and 1:5 (Fig. S6 in the supporting material of ref. 58). The latter quantity from ref. 58 is given for similar pump-laser energies per pulse and at comparable focus size as in our experiment. These yields are consistent with a rate for $Fe(CO)_4$ dissociation one order of magnitude smaller than the rate of $Fe(CO)_5$ dissociation at typical excess energies of 2-3 eV[59] as expected in solution. Furthermore, $Fe(CO)_3$ was found to arise within 5 ps (ref. 25 of the main text, no time scale for it occurrence was reported in ref. 58). In fact it can be safely assumed to arise on a similar time scale as in the gas phase (3.3 ps, ref. 17 of the main text). Solvation was found to occur on a time scale of several 10 ps[58]. Assuming a similar $Fe(CO)_3$ yield in ethanol as in heptane solution of between 1:5 and 1:10 with respect to $Fe(CO)_4$ at long times of 10-20 ps the comparably small amount having formed up to our maximum time delay of 1.7 ps can be estimated by assuming an exponential increase with a time constant of 3.3 ps to 0.4 of the maximum. With this we estimate the amount of $Fe(CO)_3$ with respect to $Fe(CO)_4$ at our maximum time delay of 1.7 ps to between 1:12.5 and 1:25 which is below our detection limit. $Fe(CO)_3$ can thus safely be neglected as a photoproduct on the time scales probed here. We therefore concentrate on the species we can robustly detect and that by far dominate our measured signals to determine their dynamics.

4. References of the Supplementary Information

31. Kunnus, K. *et al.* A setup for resonant inelastic soft x-ray scattering on liquids at free electron laser light sources. *Rev. Sci. Instrum.* **83**, 123109 (2012).

32. Heimann, P. *et al.* Linac Coherent Light Source soft x-ray materials science instrument optical design and monochromator commissioning. *Rev. Sci. Instrum.* **82**, 093104 (2011).

33. Schlotter, W.F. *et al.* The soft x-ray instrument for materials studies at the linac coherent light source x-ray free-electron laser. *Rev. Sci. Instrum.* **83**, 043107 (2012).

34. Emma, P. *et al.* First lasing and operation of an ångstrom-wavelength free-electron laser. *Nat. Photonics* **4**, 641-647 (2010).

35. Gahl, C. *et al.* A femtosecond X-ray/optical cross-correlator. *Nat. Photonics* **2**, 165-169 (2008).

36. Krupin, O. *et al.* Temporal cross-correlation of x-ray free electron and optical lasers using soft x-ray pulse induced transient reflectivity. *Optics Express* **20**, 11396-11406 (2012).

37. Myneni, S. *et al.* Spectroscopic probing of local hydrogen-bonding structures in liquid water, *J. Phys.: Condens. Matter* **14**, L213-L219 (2002).

38. Wernet, Ph. *et al.* The structure of the first coordination shell in liquid water. *Science* **304**, 995-999 (2004).

39. Rajkovic, I. *et al.* Development of a multipurpose vacuum chamber for serial optical and diffraction experiments with free electron laser radiation. *Rev. Sci. Instrum.* **81**, 045105 (2010).

40. Josefsson, I. *et al.* Ab Initio Calculations of X‑ray Spectra: Atomic Multiplet and Molecular Orbital Effects in a Multiconfigurational SCF Approach to the L‑Edge Spectra of Transition Metal Complexes. *J. Phys. Chem. Lett.* **3**, 3565-3570 (2012).

41. Malmqvist, P.A., A. Rendell, Roos, B. O., The restricted active space self-consistent-field method, implemented with a split graph unitary group approach. *J. Phys. Chem.* 94, 5477-5482 (1990).

42. Aquilante, F. *et al.* MOLCAS 7: The Next Generation. *Journal of Computational Chemistry* **31**, 224-247 (2010).

43. Douglas, M., Kroll, N. M., Quantum electrodynamical corrections to the fine structure of helium. *Annals of Physics* **82**, 89-155 (1974).

44. Hess, B. A., Relativistic electronic-structure calculations employing a two-component no-pair formalism with external-field projection operators. *Phys. Rev. A* **33**, 3742-3748 (1986).

45. Malmqvist, P.A., Roos, B.O., Schimmelpfennig, B., The restricted active space (RAS) state interaction approach with spin–orbit coupling. *Chem. Phys. Lett.* **357**, 230-240 (2002).

46. Schafer, A., Huber, C., Ahlrichs, R., Fully optimized contracted Gaussian basis sets of triple zeta valence quality for atoms Li to Kr. *J. Chem. Phys.* **100**, 5829-5835 (1994).

47. Kramers, H.A., Heisenberg, W., Über die Streuung von S trahlung durch Atome. *Zeitschritt für Physik* **31**, 681-708 (1925).

48. Ohno, M., van Riessen, G.A., *J. Electron Spectroscopy and Relat. Phenom.* **128**, 1-31 (2003).

49. Suljoti, E. *et al.* Direct observation of molecular orbital mixing in a solvated organometallic complex. *Angew. Chem. Int. Ed. Engl.* **52**, 9841-9844 (2013).

50. Dartiguenave, M., Dartiguenave, Y., Gray, H. B., Spectre électronique du fer perntacarbonyle. Étude théorique et expérimentale. *Bulletin De La Societe Chimique De France (Bull. Soc. Chim. Fr.)* **12**, 4223-4229 (1969).

51. Kotzian, M., Rösch, N., Schröder, H., Zerner, M. C., Optical Spectra of Transition-Metal Carbonyls: $Cr(CO)_6$, $Fe(CO)_5$, and $Ni(CO)_4$, *J. Am. Chem. Soc.* **111**, 7687-7696 (1989).

52. Fuß, W., Max-Planck-Institut für Quantenoptik, 85740 G arching, Germany, private communication.

53. Pierloot, K., The CASPT2 method in inorganic electronic spectroscopy: from ionic transition metal to covalent actinide complexes. *Mol. Phys.* **101**, 2083-2094 (2003).

54. Harvey, J. N., Aschi, M., Modelling spin-forbidden reactions: recombination of carbon monoxide with iron tetracarbonyl. *Faraday Discussions* **124**, 129-143 (2003).

55. González-Blanco, O., Branchadell, V., Density functional study of the Fe–CO bond dissociation energies of $Fe(CO)_5$. *J. Chem. Phys.* **110**, 778-783 (1999).

56. Lessing, J., Li, X., Lee, T., Rose-Petruck, C., Structure of Solvated $Fe(CO)_5$: Complex Formation during Solvation in Alcohols. *J. Phys. Chem. A* **112**, 2282-2292 (2008).

57. Carreón-Macedo, J.-L. , Harvey, J. N., Computational study of the energetics of $^3Fe(CO)_4$, $^1Fe(CO)_4$ and $^1Fe(CO)_4(L)$, L = Xe, CH_4, H_2 and CO. *Phys. Chem. Chem. Phys.* **8**, 93-100 (2006).

58. Nguyen, S. C., Lomont, J. P., Zoerb, M. C., Hill, A. D., Schlegel., J. P., Harris, C. B., Chemistry of the Triplet 14-Electron Complex $Fe(CO)_3$ in Solution Studied by Ultrafast Time-Resolved IR Spectroscopy. *Organometallics* **31**, 3980-3984 (2012).

59. Venkataraman, B. K., Bandukwalla, G., Zhang, Z., Vernon, M., One- and two-photon photodissociation of $Fe(CO)_5$ at 248 nm . Application of an accurate method for calculating angle resolved velocity distributions for multiple sequential bond r upture processes*J. Chem. Phys.* **90**, 5510-5526 (1989).

5. Acknowledgements of the Supplementary Information